



# Generalized stepwise optical saturation enables super-resolution fluorescence lifetime imaging microscopy

YIDE ZHANG,<sup>1,2</sup> DAVID BENIRSCHKE,<sup>1</sup> OLA ABDALSALAM,<sup>1</sup> AND SCOTT S. HOWARD<sup>1,\*</sup>

<sup>1</sup>Department of Electrical Engineering, University of Notre Dame, Notre Dame, IN 46556, USA

<sup>2</sup>yzhang34@nd.edu

\*showard@nd.edu

**Abstract:** We present a novel super-resolution fluorescence lifetime microscopy technique called generalized stepwise optical saturation (GSOS) that generalizes and extends the concept of the recently demonstrated stepwise optical saturation (SOS) super-resolution microscopy [Biomed. Opt. Express **9**, 1613 (2018)]. The theoretical basis of GSOS is developed based on exploring the dynamics of a two-level fluorophore model and using perturbation theory. We show that although both SOS and GSOS utilize the linear combination of  $M$  raw images to increase the imaging resolution by a factor of  $\sqrt{M}$ , SOS is a special and the simplest case of GSOS. The super-resolution capability is demonstrated with theoretical analysis and numerical simulations for GSOS with sinusoidal and pulse-train modulations. Using GSOS with pulse-train modulation, super-resolution and fluorescence lifetime imaging microscopy (FLIM) images can be obtained simultaneously. The super-resolution FLIM capability is experimentally demonstrated with a cell sample on a custom-built two-photon frequency-domain (FD) FLIM system based on radio frequency analog signal processing. To our knowledge, this is the first implementation of super-resolution imaging in FD-FLIM.

© 2018 Optical Society of America under the terms of the [OSA Open Access Publishing Agreement](#)

**OCIS codes:** (100.6640) Superresolution; (170.2520) Fluorescence microscopy; (170.3650) Lifetime-based sensing; (180.4315) Nonlinear microscopy; (190.4180) Multiphoton processes.

## References and links

1. S. W. Hell, "Far-field optical nanoscopy," *Science* **316**, 1153–1158 (2007).
2. S. W. Hell and J. Wichmann, "Breaking the diffraction resolution limit by stimulated emission: stimulated-emission-depletion fluorescence microscopy," *Opt. Lett.* **19**, 780–782 (1994).
3. E. Betzig, G. H. Patterson, R. Sougrat, O. W. Lindwasser, S. Olenych, J. S. Bonifacino, M. W. Davidson, J. Lippincott-Schwartz, and H. F. Hess, "Imaging intracellular fluorescent proteins at nanometer resolution," *Science* **313**, 1642–1645 (2006).
4. M. J. Rust, M. Bates, and X. Zhuang, "Sub-diffraction-limit imaging by stochastic optical reconstruction microscopy (STORM)," *Nat. Methods* **3**, 793–796 (2006).
5. M. G. L. Gustafsson, "Nonlinear structured-illumination microscopy: Wide-field fluorescence imaging with theoretically unlimited resolution," *Proc. Natl. Acad. Sci. USA* **102**, 13081–13086 (2005).
6. K. Fujita, M. Kobayashi, S. Kawano, M. Yamanaka, and S. Kawata, "High-resolution confocal microscopy by saturated excitation of fluorescence," *Phys. Rev. Lett.* **99**, 228105 (2007).
7. J. Humpolíčková, A. Benda, and J. Enderlein, "Optical saturation as a versatile tool to enhance resolution in confocal microscopy," *Biophys. J.* **97**, 2623–2629 (2009).
8. Y. Zhang, P. D. Nallathamby, G. D. Vigil, A. A. Khan, D. E. Mason, J. D. Boerckel, R. K. Roeder, and S. S. Howard, "Super-resolution fluorescence microscopy by stepwise optical saturation," *Biomed. Opt. Express* **9**, 1613–1629 (2018).
9. Y. Zhang, D. Benirschke, and S. S. Howard, "Stepwise optical saturation microscopy: obtaining super-resolution images with conventional fluorescence microscopes," in "Biophotonics Congress: Biomedical Optics Congress 2018," (OSA, 2018), p. JTh3A.27.
10. H. C. Gerritsen, A. Draaijer, D. J. van den Heuvel, and A. V. Agronskaia, "Fluorescence lifetime imaging in scanning microscopy," in "Handbook Of Biological Confocal Microscopy," J. Pawley, ed. (Springer US, Boston, MA, 2006), pp. 516–534, 3rd ed.

11. C.-W. Chang, D. Sud, and M.-A. Mycek, "Fluorescence lifetime imaging microscopy," *Method. Cell Biol.* **81**, 495–524 (2007).
12. D. O'Connor, *Time-Correlated Single Photon Counting* (Academic Press, 2012).
13. C. J. De Grauw and H. C. Gerritsen, "Multiple time-gate module for fluorescence lifetime imaging," *Appl. Spectrosc.* **55**, 670–678 (2001).
14. Y. Sun, R. N. Day, and A. Periasamy, "Investigating protein-protein interactions in living cells using fluorescence lifetime imaging microscopy," *Nat. Protoc.* **6**, 1324–1340 (2011).
15. T. Hato, S. Winfree, R. Day, R. M. Sandoval, B. A. Molitoris, M. C. Yoder, R. C. Wiggins, Y. Zheng, K. W. Dunn, and P. C. Dagher, "Two-photon intravital fluorescence lifetime imaging of the kidney reveals cell-type specific metabolic signatures," *J. Am. Soc. Nephrol.* **28**, 2420–2430 (2017).
16. Y. Zhang, A. A. Khan, G. D. Vigil, and S. S. Howard, "Super-sensitivity multiphoton frequency-domain fluorescence lifetime imaging microscopy," *Opt. Express* **24**, 20862–20867 (2016).
17. Y. Zhang, G. D. Vigil, L. Cao, A. A. Khan, D. Benirschke, T. Ahmed, P. Fay, and S. S. Howard, "Saturation-compensated measurements for fluorescence lifetime imaging microscopy," *Opt. Lett.* **42**, 155–158 (2017).
18. E. Auksoorius, B. R. Boruah, C. Dunsby, P. M. P. Lanigan, G. Kennedy, M. A. A. Neil, and P. M. W. French, "Stimulated emission depletion microscopy with a supercontinuum source and fluorescence lifetime imaging," *Opt. Lett.* **33**, 113–115 (2008).
19. J. Bückers, D. Wildanger, G. Vicidomini, L. Kastrup, and S. W. Hell, "Simultaneous multi-lifetime multi-color STED imaging for colocalization analyses," *Opt. Express* **19**, 3130–3143 (2011).
20. M. D. Lesoine, S. Bose, J. W. Petrich, and E. A. Smith, "Supercontinuum stimulated emission depletion fluorescence lifetime imaging," *J. Phys. Chem. B* **116**, 7821–7826 (2012).
21. F. Görlitz, D. Corcoran, E. Garcia Castano, B. Leitinger, M. Neil, C. Dunsby, and P. French, "Mapping molecular function to biological nanostructure: combining structured illumination microscopy with fluorescence lifetime imaging (SIM + FLIM)," *Photonics* **4**, 40 (2017).
22. J. Philip and K. Carlsson, "Theoretical investigation of the signal-to-noise ratio in fluorescence lifetime imaging," *J. Opt. Soc. Am. A* **20**, 368–379 (2003).
23. C. Eggeling, A. Volkmer, and C. A. M. Seidel, "Molecular photobleaching kinetics of rhodamine 6G by one- and two-photon induced confocal fluorescence microscopy," *ChemPhysChem* **6**, 791–804 (2005).
24. C. Xu and W. W. Webb, "Measurement of two-photon excitation cross sections of molecular fluorophores with data from 690 to 1050 nm," *J. Opt. Soc. Am. B* **13**, 481–491 (1996).
25. R. W. Boyd, *Nonlinear Optics* (Academic Press, 2003).
26. S. R. Kurtz, "Mixers as phase detectors," *Watkins-Johnson Tech-Notes* **5** (1978).
27. N. Boens, W. Qin, N. Basarić, J. Hofkens, M. Ameloot, J. Pouget, J.-P. Lefèvre, B. Valeur, E. Gratton, M. VandeVen, N. D. Silva, Y. Engelborghs, K. Willaert, A. Sillen, G. Rumbles, D. Phillips, A. J. W. G. Visser, A. van Hoek, J. R. Lakowicz, H. Malak, I. Gryczynski, A. G. Szabo, D. T. Krajcarski, N. Tamai, and A. Miura, "Fluorescence lifetime standards for time and frequency domain fluorescence spectroscopy," *Anal. Chem.* **79**, 2137–2149 (2007).
28. A. S. Kristoffersen, S. R. Erga, B. Hamre, and Ø. Frette, "Testing fluorescence lifetime standards using two-photon excitation and time-domain instrumentation: rhodamine B, coumarin 6 and lucifer yellow," *J. Fluoresc.* **24**, 1015–1024 (2014).
29. R. M. Zucker, "Quality assessment of confocal microscopy slide based systems: Performance," *Cytometry Part A* **69A**, 659–676 (2006).

## 1. Introduction

Super-resolution fluorescence microscopy techniques have enabled a dramatic development in modern biology by being able to discern fluorescent features that are smaller than the diffraction limit [1–9] and can be achieved using a variety of techniques such as stimulated emission depletion (STED) microscopy [2], photoactivated localization microscopy (PALM) [3], stochastic optical reconstruction microscopy (STORM) [4], structured illumination microscopy (SIM) [5], saturated excitation (SAX) microscopy [6, 7], and the recently demonstrated stepwise optical saturation (SOS) microscopy [8, 9]. Fluorescence lifetime imaging microscopy (FLIM) is also a powerful tool in biomedical research by imaging an additional contrast, the fluorescence decay lifetime of excited fluorophores, which enables the measurement of important information such as the ion concentration, the dissolved oxygen concentration, the pH, and the refractive index, about the microenvironment in living tissues [10–17]. FLIM methods are generally divided into two categories: time-domain (TD) FLIM, such as time-correlated signal photon counting (TCSPC) and time-gating (TG) [12, 13], and frequency-domain (FD) FLIM [14–17]. Super-resolution and FLIM techniques can be combined into an integrated system, which is attractive for its capability to measure the microenvironment in living tissues with a subdiffraction

resolution. Super-resolution FLIM has been realized solely in TD-FLIM by combining STED with TCSPC [18–20] or by integrating SIM with TG [21]. No previous research, however, has implemented super-resolution imaging in FD-FLIM, which is preferred in many cases for its rapid acquisition, easy implementation, and reduced bandwidth requirements [22].

In this work, we present a novel microscopy technique, termed generalized stepwise optical saturation (GSOS), that is able to generate super-resolution lifetime images using FD-FLIM approaches. The GSOS microscopy is a generalization of the recently demonstrated SOS microscopy [8, 9]. Similar to SOS, GSOS utilizes the linear combination of  $M$  steps of raw images to improve the imaging resolution by a factor of  $\sqrt{M}$ . While SOS employs Taylor expansion and assumes the steady-state solution of a two-level fluorophore model, GSOS uses perturbation theory and explores the full dynamics of the model; therefore GSOS can generate super-resolution images as well as extract the lifetime information hidden in the dynamics of the system. We show with theory and simulations that both sinusoidal and pulse-train signals can be used as the excitation source in GSOS microscopy to generate super-resolution images, where pulse-train modulation is preferred for it can greatly simplify the lifetime measurement process in practice. We finally experimentally demonstrate the super-resolution FLIM capability enabled by GSOS with pulse-train modulation on a custom-built two-photon FD-FLIM system based on a low-cost, high-performance homodyne detection method using radio frequency (RF) analog signal processing.

## 2. Generalized stepwise optical saturation based on perturbation theory

The GSOS microscopy is based on the same two-level fluorophore model used in the SOS microscopy [8]:

$$\frac{dF(t)}{dt} = KN_0g_p\sigma_N\gamma^N I^N(t) - \left(g_p\sigma_N\gamma^N I^N(t) + \frac{1}{\tau}\right) F(t), \quad (1)$$

where  $I(t)$  and  $F(t)$  are the excitation irradiance and fluorescence intensity, respectively, as functions of time;  $K = \psi_F t_{ob}/\tau$  where  $\tau$  is the fluorescence lifetime,  $\psi_F$  the fluorescence detection efficiency, and  $t_{ob}$  the observation time;  $N$  is the number of excitation photons needed for a fluorophore to emit one photon [ $N = 1$  for one-photon excitation fluorescence (1PEF),  $N = 2$  for two-photon excitation fluorescence (2PEF), etc.];  $N_0$  is the concentration of the fluorophore;  $g_p$  is the pulse gain factor which accounts for the temporal pulse profile of the excitation [23, 24];  $\sigma_N$  is the cross-section for  $N$ -photon excitation;  $\gamma = \lambda_{exc}/(hc)$  where  $h$  is Planck's constant,  $c$  the velocity of light, and  $\lambda_{exc}$  the excitation wavelength. It is difficult to obtain a closed-form solution to Eq. (1). In SOS microscopy [8], we assumed a steady-state solution to Eq. (1). In GSOS, however, the steady-state assumption cannot be used for we need to consider the dynamics of the model. In order to solve Eq. (1) and utilize its dynamics, we use the perturbation techniques [25]. We introduce an expansion parameter  $\lambda$  which is assumed to vary continuously between zero and one. The value  $\lambda = 1$  is correspondent to the physical situation. We replace  $I^N(t)$  by  $\lambda I^N(t)$  in Eq. (1) and expand  $F(t)$  in powers of the interaction as

$$F(t) = F^{(0)} + \lambda F^{(1)} + \lambda^2 F^{(2)} + \lambda^3 F^{(3)} + \dots \quad (2)$$

By equating powers of  $\lambda$  on each side of the resulting form of Eq. (1), we obtain a set of equations:

$$\lambda^0 : \frac{dF^{(0)}(t)}{dt} = -\frac{1}{\tau}F^{(0)}(t), \quad (3)$$

$$\lambda^1 : \frac{dF^{(1)}(t)}{dt} = KN_0g_p\sigma_N\gamma^N I^N(t) - g_p\sigma_N\gamma^N I^N(t)F^{(0)}(t) - \frac{1}{\tau}F^{(1)}(t), \quad (4)$$

$$\lambda^2 : \frac{dF^{(2)}(t)}{dt} = -g_p\sigma_N\gamma^N I^N(t)F^{(1)}(t) - \frac{1}{\tau}F^{(2)}(t), \quad (5)$$

$$\lambda^3 : \frac{dF^{(3)}(t)}{dt} = -g_p\sigma_N\gamma^N I^N(t)F^{(2)}(t) - \frac{1}{\tau}F^{(3)}(t), \quad (6)$$

$$\vdots$$

$$\lambda^n : \frac{dF^{(n)}(t)}{dt} = -g_p\sigma_N\gamma^N I^N(t)F^{(n-1)}(t) - \frac{1}{\tau}F^{(n)}(t), \quad (n \geq 2). \quad (7)$$

In GSOS microscopy, the excitation irradiance  $I(t)$  is modulated by a periodic signal. The modulation can be implemented by instruments such as a mechanical chopper, an electro-optic modulator (EOM), or an acousto-optic modulator (AOM); the modulated excitation can also be the inherent femtosecond pulses in a mode-locked laser. Governed by the system in Eq. (1), both  $I^N(t)$  and  $F(t)$  are also periodic and possess the same angular modulation frequency  $\omega$  and period  $T$  ( $T = 2\pi/\omega$ ) with  $I(t)$ . Based on the periodicity of  $I^N(t)$ , we can describe it with Fourier series

$$I^N(t) = \bar{I}^N \sum_{k=-\infty}^{\infty} p_k \exp(ik\omega t), \quad p_k = \frac{1}{T} \int_0^T \frac{I^N(t)}{\bar{I}^N} \exp(-ik\omega t) dt, \quad (8)$$

where  $\bar{I}^N = \int_0^T I^N(t) dt / T$ , which is used to normalized the excitation power such that  $p_0 = 1$ . Similarly, we can describe  $F(t)$  with Fourier series

$$F(t) = \sum_{k=-\infty}^{\infty} q_k \exp(ik\omega t), \quad q_k = \frac{1}{T} \int_0^T F(t) \exp(-ik\omega t) dt, \quad (9)$$

Based on Eq. (2), the Fourier coefficients  $q_k$  of  $F(t)$  can also be written as

$$q_k = q_k^{(0)} + \lambda q_k^{(1)} + \lambda^2 q_k^{(2)} + \lambda^3 q_k^{(3)} + \dots, \quad (10)$$

and for each order of interaction, we have

$$F^{(n)}(t) = \sum_{k=-\infty}^{\infty} q_k^{(n)} \exp(ik\omega t), \quad q_k^{(n)} = \frac{1}{T} \int_0^T F^{(n)}(t) \exp(-ik\omega t) dt. \quad (11)$$

Note that all the Fourier coefficients  $p_k$ ,  $q_k$ , and  $q_k^{(n)}$  are complex numbers.

### 2.1. Zero-order interaction

The zero-order interaction ( $n = 0$ ) is described with Eq. (3). We assume  $F^{(0)}(0) = 0$  since no excitation is added before  $t = 0$ , so  $F^{(0)}(t) = 0$  for  $t \geq 0$ , and correspondingly  $q_k^{(0)} = 0$ .

### 2.2. First-order interaction

The first-order interaction ( $n = 1$ ) is described with Eq. (4). Since  $F^{(0)}(t) = 0$ , we have

$$\frac{dF^{(1)}(t)}{dt} = KN_0g_p\sigma_N\gamma^N I^N(t) - \frac{1}{\tau}F^{(1)}(t). \quad (12)$$

With Eqs. (8) and (11), we know

$$\sum_{l=-\infty}^{\infty} \left( q_l^{(1)} \frac{1 + il\omega\tau}{\tau} \right) \exp(il\omega t) = KN_0 g_p \sigma_N \gamma^N \bar{I}^N \sum_{m=-\infty}^{\infty} p_m \exp(im\omega t). \quad (13)$$

Therefore, for the Fourier coefficients with index  $k$ , denoting  $a = \tau g_p \sigma_N \gamma^N$ , we have

$$q_k^{(1)} = KN_0 a \bar{I}^N \left( \frac{1}{1 + ik\omega\tau} p_k \right). \quad (14)$$

This result is as expected and used conventionally in FD-FLIM, when excitation is far from saturation, to extract the lifetime [10].

### 2.3. Second-order interaction

The second-order interaction ( $n = 2$ ) is described with Eq. (5). With Eqs. (8) and (11), we have

$$\sum_{l=-\infty}^{\infty} \left( q_l^{(2)} \frac{1 + il\omega\tau}{\tau} \right) \exp(il\omega t) = -g_p \sigma_N \gamma^N \bar{I}^N \sum_{m=-\infty}^{\infty} \sum_{l=-\infty}^{\infty} p_m q_l^{(1)} \exp(i(l + m)\omega t). \quad (15)$$

For the Fourier coefficients with index  $k$ , we get

$$q_k^{(2)} = -\frac{\tau}{1 + ik\omega\tau} g_p \sigma_N \gamma^N \bar{I}^N \left[ p_k * q_k^{(1)} \right]. \quad (16)$$

where  $\left[ p_k * q_k^{(1)} \right] = \sum_{j=-\infty}^{\infty} p_{k-j} q_j^{(1)}$  is the discrete convolution between the coefficients  $p_k$  and  $q_k^{(1)}$ . With Eq. (14), Eq. (16) can be written as

$$q_k^{(2)} = -KN_0 a^2 \bar{I}^{2N} \left( \frac{1}{1 + ik\omega\tau} \left[ p_k * \left( \frac{1}{1 + ik\omega\tau} p_k \right) \right] \right). \quad (17)$$

### 2.4. Third-order interaction

The third-order interaction ( $n = 3$ ) is described with Eq. (6). With Eqs. (8) and (11), we have

$$\sum_{l=-\infty}^{\infty} \left( q_l^{(3)} \frac{1 + il\omega\tau}{\tau} \right) \exp(il\omega t) = -g_p \sigma_N \gamma^N \bar{I}^N \sum_{m=-\infty}^{\infty} \sum_{l=-\infty}^{\infty} p_m q_l^{(2)} \exp(i(l + m)\omega t). \quad (18)$$

Similarly, for the coefficients with index  $k$ , we have

$$q_k^{(3)} = -\frac{\tau}{1 + ik\omega\tau} g_p \sigma_N \gamma^N \bar{I}^N \left[ p_k * q_k^{(2)} \right]. \quad (19)$$

With Eq. (17), Eq. (19) can be written as

$$q_k^{(3)} = KN_0 a^3 \bar{I}^{3N} \left( \frac{1}{1 + ik\omega\tau} \left[ p_k * \left( \frac{1}{1 + ik\omega\tau} \left[ p_k * \left( \frac{1}{1 + ik\omega\tau} p_k \right) \right] \right) \right] \right), \quad (20)$$

### 2.5. $n$ -th-order interaction

The  $n$ -th-order interaction ( $n \geq 2$ ) is described with Eq. (7). With Eqs. (8) and (11), we have

$$\sum_{l=-\infty}^{\infty} \left( q_l^{(n)} \frac{1 + il\omega\tau}{\tau} \right) \exp(il\omega t) = -g_p \sigma_N \gamma^N \bar{I}^N \sum_{m=-\infty}^{\infty} \sum_{l=-\infty}^{\infty} p_m q_l^{(n-1)} \exp(i(l + m)\omega t). \quad (21)$$

For the index  $k$ , we know

$$q_k^{(n)} = -\frac{\tau}{1 + ik\omega\tau} g_p \sigma_N \gamma^N \bar{I}^N \left[ p_k * q_k^{(n-1)} \right]. \quad (22)$$

In a manner similar to Eqs. (14), (17), and (20), Eq. (22) can be written as

$$q_k^{(n)} = KN_0 (-1)^{n+1} a^n \bar{I}^N \left( \frac{1}{1 + ik\omega\tau} \left[ p_k * \left( \frac{1}{1 + ik\omega\tau} \left[ p_k * \left( \cdots \right) \right] \right) \right] \right). \quad (23)$$

In summary, based on Eqs. (14), (17), (20), and (23), in physical situations where  $\lambda = 1$ ,  $q_k$ , the Fourier coefficient of  $F(t)$ , can be written as

$$q_k = q_k^{(1)} + q_k^{(2)} + q_k^{(3)} + \cdots, \quad (24)$$

which can be interpreted as that the complex fluorescence response of the  $k$ -th harmonic,  $q_k$ , is the unsaturated response  $q_k^{(1)}$  plus high-order correction terms that occur at high-excitation intensities due to saturation.

### 3. Principle of GSOS microscopy

Here we consider one-dimensional spatial dependence of excitation and fluorescence. The extension to a multi-dimensional case is trivial. Based on Eq. (8), we assume  $I^N(t, x) = \bar{I}^N(x) \sum_{k=-\infty}^{\infty} p_k \exp(ik\omega t)$  and  $p_k = \int_0^T [I^N(t, x)/\bar{I}^N(x)] \exp(-ik\omega t) dt/T$ , where a Gaussian excitation profile is assumed in the focus;  $\bar{I}(x) = I_0 \exp(-2x^2/W_0^2)$  with the focal irradiance  $I_0 = \bar{I}(x = 0)$  and  $1/e^2$  radius  $W_0$ . In the case of  $N$ -photon excitation, this profile is effectively powered to the  $N$ -th as  $\bar{I}^N(x)$ . We can separate the spatial dependency by denoting  $g(x) = \exp(-2x^2/\omega^2)$  and we have  $\bar{I}^N(x) = I_0^N g^N(x)$ . Identically, based on Eq. (9), we assume  $F(t, x) = \sum_{k=-\infty}^{\infty} q_k(x) \exp(ik\omega t)$  and  $q_k(x) = \int_0^T F(t, x) \exp(-ik\omega t) dt/T$ . Then, with Eq. (24), we have

$$\begin{aligned} q_k(x) = & KN_0 \left\{ a I_0^N g^N(x) \left( \frac{1}{1 + ik\omega\tau} p_k \right) \right. \\ & - a^2 I_0^{2N} g^{2N}(x) \left( \frac{1}{1 + ik\omega\tau} \left[ p_k * \left( \frac{1}{1 + ik\omega\tau} p_k \right) \right] \right) \\ & \left. + a^3 I_0^{3N} g^{3N}(x) \left( \frac{1}{1 + ik\omega\tau} \left[ p_k * \left( \frac{1}{1 + ik\omega\tau} \left[ p_k * \left( \frac{1}{1 + ik\omega\tau} p_k \right) \right] \right) \right] \right) - \cdots \right\}. \end{aligned} \quad (25)$$

As an  $M$ -step SOS microscopy needs  $M$  fluorescence images to be collected, an  $M$ -step GSOS (M-GSOS) microscopy requires  $M$  steps of harmonic images  $q_k$  to be obtained. A subscript  $m$  is added to the excitation and fluorescence intensities and Fourier coefficients of the  $m$ -th step image among the  $M$  images. Then for the  $m$ -th step, Eq. (25) can be written as

$$\begin{aligned} q_{k,m}(x) = & KN_0 \left\{ a I_{0m}^N g^N(x) \left( \frac{1}{1 + ik\omega\tau} p_k \right) \right. \\ & - a^2 I_{0m}^{2N} g^{2N}(x) \left( \frac{1}{1 + ik\omega\tau} \left[ p_k * \left( \frac{1}{1 + ik\omega\tau} p_k \right) \right] \right) \\ & \left. + a^3 I_{0m}^{3N} g^{3N}(x) \left( \frac{1}{1 + ik\omega\tau} \left[ p_k * \left( \frac{1}{1 + ik\omega\tau} \left[ p_k * \left( \frac{1}{1 + ik\omega\tau} p_k \right) \right] \right) \right] \right) - \cdots \right\}. \end{aligned} \quad (26)$$

In Eq. (26), high powers of  $g^N(x)$ , such as  $g^{2N}(x)$ ,  $g^{3N}(x)$ , etc., represent components with higher spatial frequency, while  $g^N(x)$  is the diffraction-limited component. With the definition



Table 1. Coefficients for the linear combination in SOS and GSOS microscopy.

Coefficients		Expressions
Two-step	$c_1$	$\frac{1}{I_{01}^N}$
	$c_2$	$-\frac{I_{01}^N}{I_{02}^N}$
Three-step	$c_1$	$\frac{1}{I_{01}^N(I_{01}^N - I_{03}^N)}$
	$c_2$	$-\frac{I_{01}^N(I_{01}^N - I_{03}^N)}{I_{02}^N(I_{02}^N - I_{03}^N)}$
	$c_3$	$\frac{I_{01}^N(I_{01}^N - I_{02}^N)}{I_{03}^N(I_{02}^N - I_{03}^N)}$

of  $g(x)$ , an  $M$ -th order power component,  $g^{MN}(x)$ , has a  $\sqrt{M}$ -fold increase in spatial resolution. Due to the magnitude difference among each components, the spatial resolution of  $q_{k,m}(x)$  is dominated by the lowest power of  $g^N(x)$ .

The concept of  $M$ -step GSOS microscopy is to eliminate the lowest  $M - 1$  powers of  $g^N(x)$  by the linear combination of  $M$  steps of fluorescence harmonic images,  $q_{k,m}(x)$ , obtained at different excitation intensities. We assume the excitation intensities of each step follow  $I_{01} < I_{02} < \dots < I_{0M}$ . The resulting GSOS image of the  $k$ -th fluorescence harmonic is

$$q_{k,M\text{-GSOS}}(x) = \sum_{m=1}^M c_m q_{k,m}(x), \quad (27)$$

where the coefficients  $c_m$  are chosen such that the lowest power of  $g^N(x)$  in  $q_{k,M\text{-GSOS}}(x)$  is  $g^{MN}(x)$ . In other words, an  $M$ -step GSOS image will have a  $\sqrt{M}$ -fold increase in spatial resolution. The coefficients  $c_m$  for different types of GSOS methods and how they are obtained are identical to the ones described in the SOS paper [8]. Here we present them in Tab. 1 again for convenience. For example, in two-step SOS, we need two images,  $q_{k,1}(x)$  and  $q_{k,2}(x)$ , obtained at excitation intensities,  $I_{01}$  and  $I_{02}$ , respectively. With the power series in Eq. (26) and the two-step coefficients,  $c_1$  and  $c_2$ , in Tab. 1, the resulting two-step GSOS image is

$$\begin{aligned} q_{k,2\text{-GSOS}}(x) &= c_1 q_{k,1}(x) + c_2 q_{k,2}(x) \\ &= KN_0 \left\{ -a^2 I_{01}^N (I_{01}^N - I_{02}^N) g^{2N}(x) \left( \frac{1}{1 + ik\omega\tau} \left[ p_k * \left( \frac{1}{1 + ik\omega\tau} p_k \right) \right] \right) \right. \\ &\quad \left. + a^3 I_{01}^N (I_{01}^{2N} - I_{02}^{2N}) g^{3N}(x) \right. \\ &\quad \left. \times \left( \frac{1}{1 + ik\omega\tau} \left[ p_k * \left( \frac{1}{1 + ik\omega\tau} \left[ p_k * \left( \frac{1}{1 + ik\omega\tau} p_k \right) \right] \right) \right] \right) - \dots \right\}. \end{aligned} \quad (28)$$

which is dominated by the component  $g^{2N}(x)$ . Compared to the diffraction-limited component  $g^N(x)$ ,  $q_{k,2\text{-GSOS}}(x)$  therefore has a  $\sqrt{2}$ -fold increase in spatial resolution.

#### 4. SOS: a special case of GSOS microscopy

In a GSOS microscope, the excitation irradiance  $I(t)$  is modulated by a periodic signal with angular modulation frequency  $\omega$ . If  $\omega = 0$ , then  $I^N(t)$  and  $F(t)$  in GSOS will be DC (constant) signals and Eq. (1) can be easily solved with a steady-state solution, which is the method we used in the SOS paper [8]. Therefore, based on Eqs. (8) and (9), we will have  $I^N(t) = \bar{I}^N p_0 = \bar{I}^N$  and  $F(t) = q_0$ . Consequently, based on Eq. (25), with  $k = 0$ ,  $\omega = 0$ , and  $p_0 = 1$ , the fluorescence signal in a GSOS microscope becomes

$$F(x) = q_0(x) = KN_0 \{ a I_0^N g^N(x) - a^2 I_0^{2N} g^{2N}(x) + a^3 I_0^{3N} g^{3N}(x) - \dots \}, \quad (29)$$

which is real and identical to the form in the SOS paper [8]. In summary, since  $\omega$  can be of any non-negative value in a GSOS microscope, the previously demonstrated SOS technique, which corresponds to  $\omega = 0$ , is simply a special case of the GSOS microscopy.

## 5. GSOS microscopy with sinusoidal modulation

In conventional two-photon microscopy, periodic modulation on the excitation source is generally implemented with an EOM/AOM controlled by a function generator [16, 17]. Typically, the EOM/AOM is modulated by a sinusoidal signal  $I(t) = A[1 + m \sin(\omega t)]$ , where  $A$  is the average amplitude of the signal,  $m$  the modulation degree  $0 < m \leq 1$ , and  $\omega$  the angular frequency. Based on Eq. (8), the harmonics of the 2PEF ( $N = 2$ ) are  $p_0 = 1$ ,  $p_1 = \overline{p_{-1}} = -2mi/(m^2 + 2)$ ,  $p_2 = \overline{p_{-2}} = -m^2/(2m^2 + 4)$  and  $\overline{I^2} = A^2(m^2 + 2)/2$ . However, considering the infinite terms and complicated convolution operations in Eq. (25), the fluorescence harmonics  $q_k$  cannot be analytically derived in this case. We perform simulations to acquire the dynamics of  $q_k$  numerically in order to apply GSOS methods on the simulated results. The simulation is based on numerically solving Eq. (1) in Matlab (MathWorks) with the periodic excitation  $I(t)$ . The solved fluorescence signal  $F(t)$  is fast Fourier transformed to acquire its harmonics  $q_k$ . This process is performed repeatedly with different excitation irradiances  $\bar{I}$ . The simulation parameters are set as follows:  $\tau = 3$  ns,  $f_{\text{mod}} = 80$  MHz,  $\omega = 2\pi f_{\text{mod}}$ ,  $\lambda_{\text{exc}} = 800$  nm,  $g_p = 38690$ ,  $\sigma_2 = 2 \times 10^{-56}$  m<sup>4</sup>s, NA = 0.8,  $W_0 = \lambda_{\text{exc}}/(\pi \text{NA})$ ,  $t_{ob} = 24.4$  ps,  $\psi_F = 0.02$ ,  $N_0 = 1$ ,  $h = 6.626 \times 10^{-34}$  J · s,  $c = 3 \times 10^8$  m/s,  $m = 1$ . Simulated one-dimensional complex point spread functions (PSFs) consist of 256 pixels with a pixel width of 8 nm. Two-step GSOS (2-GSOS) and three-step GSOS (3-GSOS) complex PSFs are obtained by linear combining diffraction-limited (DL) complex PSFs simulated with different excitation irradiances:  $I_{01} = 50$  GW/m<sup>2</sup>,  $I_{02} = 1.2I_{01}$ ,  $I_{03} = 1.4I_{01}$ .

The simulated results are presented in Fig. 1. With different excitation irradiances  $\bar{I}$ , the DC ( $q_0$ ),  $1\omega$  ( $q_1$ ), and  $2\omega$  ( $q_2$ ) fluorescence harmonics show different trajectories on the complex plane [Fig. 1(a)] and distinct magnitude and phase behaviors [Fig. 1(b)].  $q_0$  are consistently real and exhibit saturation behavior under high excitation irradiances; this is the basis of SOS microscopy which solely relies on the saturation of fluorescence intensity (DC) [8].  $q_1$ , on the other hand, starts with a constant initial phase related to the fluorescence lifetime but as saturation happens, the magnitude and phase both change; this is consistent with the phenomenon we reported in [17] that in FD-FLIM, high excitation irradiances led to fluorophore saturation which in turn caused incorrect lifetime measurements.  $q_2$  also begins with a constant initial phase but the deviation due to saturation starts at a even lower excitation irradiance. Although these harmonics (other than DC) cannot be analytically described in a closed-form, they are all governed by Eq. (25) based on perturbation theory. Figures 1(c) and 1(d) present simulated magnitude and phase of complex PSFs of DC,  $1\omega$ , and  $2\omega$  harmonics for DL, 2-GSOS, and 3-GSOS. Compared to DL, resolution improvements in magnitude PSFs of 2-GSOS and 3-GSOS can be clearly seen for all DC,  $1\omega$ , and  $2\omega$  harmonics. This could not happen if  $q_k$  were not governed by Eq. (25). According to Eqs. (25) and (27),  $g^{2N}(x)$  and  $g^{3N}(x)$  become the dominant terms for 2-GSOS and 3-GSOS, respectively, which correspond to a  $\sqrt{2}$  and  $\sqrt{3}$  folds magnitude resolution improvement over  $g^N(x)$  that dominates in the DL [Fig. 1(c)]. The phase PSFs shown in Fig. 1(d) demonstrate a unpredictable behavior for GSOS methods with sinusoidal modulation due to complicated phase dynamics under fluorophore saturation. Note that in the phase PSFs only the pixels with a magnitude larger than 0.1% of the peak value (magnitude at  $x = 0$ ) are plotted because pixels with a magnitude smaller than 0.1% exhibit fluctuating phase readings due to limited numerical accuracy in Matlab. The phase fluctuation can still be seen in 3-GSOS phase PSFs for  $1\omega$  and  $2\omega$  harmonics. Although these phases contain the information of fluorescence lifetime  $\tau$  according to Eqs. (25) and (27), due to the complicated phase dynamics in GSOS microscopy with sinusoidal modulation, the lifetime cannot be retrieved directly. This shortcoming can be overcome using pulse-train modulation, as described below.



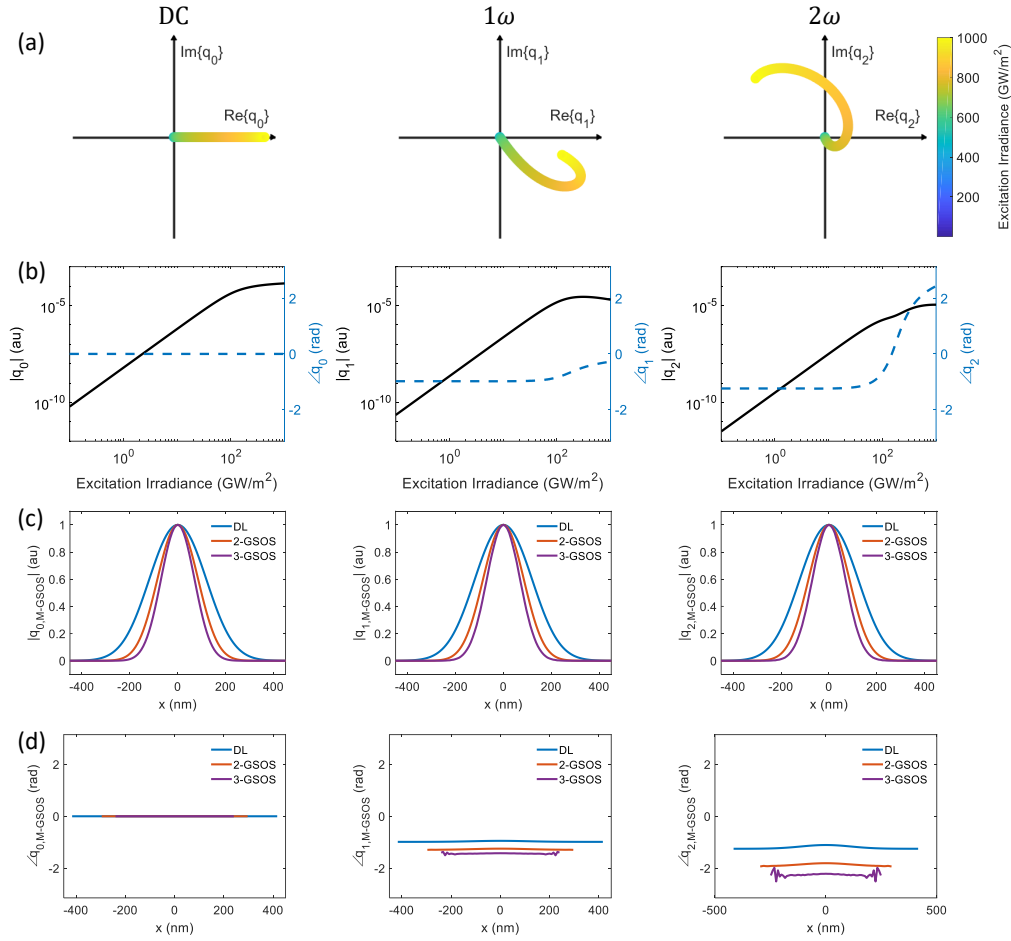


Fig. 1. Simulated results for GSOS microscopy with sinusoidal modulation. (a) Complex trajectories and (b) magnitude and phase of fluorescence harmonics  $q_k$  with different excitation irradiances. (c) Magnitude and (d) phase of complex PSFs of diffraction-limited (DL), two-step, and three-step GSOS microscopy.

## 6. GSOS microscopy with pulse-train modulation

As shown in Eq. (8), the excitation irradiance  $I(t)$  in a GSOS microscope can be any periodic signal. The Ti:sapphire laser used in a two-photon microscope is a mode-locked laser generating periodic femtosecond pulses at 80 MHz, which is an intrinsically modulated excitation source. In fact, the pulses (femtosecond) are so short compared with the modulation period [ $T = 1/(80 \text{ MHz}) = 12.5 \text{ ns}$ ] that we can consider these pulses as perfect Delta functions. Mathematically, this is  $I(t) = A\delta_T$ , where  $A$  is a coefficient related to the average power of the excitation. With two-photon microscopy, we have  $N = 2$ , and  $I^2(t) = A^2\delta_T$ . Note that the square of a Delta function is also a Delta function. Hence, based on Eqs. (8), we have  $\bar{I}^2 = A^2/T$  and  $p_k = 1$ . Note that all the Fourier coefficients of the excitation  $I^2(t)$  are constant and equal to one, which will greatly simplify the math, especially the convolution, in GSOS microscopy.

With  $p_k = 1$ , based on Eq. (14), we have the first-order interaction as

$$q_k^{(1)} = KN_0a\bar{I}^N \frac{1}{1 + ik\omega\tau}. \quad (30)$$

Then, for the second-order interaction, based on Eq. (16),

$$q_k^{(2)} = -a\bar{I}^N \frac{1}{1 + ik\omega\tau} \left[ p_k * q_k^{(1)} \right], \quad (31)$$

where the convolution term, with Eq. (30), becomes

$$\left[ p_k * q_k^{(1)} \right] = \sum_{j=-\infty}^{\infty} p_{k-j} q_j^{(1)} = \sum_{j=-\infty}^{\infty} q_j^{(1)} = KN_0 a \bar{I}^N \sum_{j=-\infty}^{\infty} \frac{1}{1 + ij\omega\tau}. \quad (32)$$

The sum of the series can be simplified by grouping complex conjugate pairs into

$$\sum_{j=-\infty}^{\infty} \frac{1}{1 + ij\omega\tau} = 1 + \sum_{m=1}^{\infty} \frac{2}{1 + (m\omega\tau)^2}, \quad (33)$$

which is convergent based on the physical situation and the result is a real number. By assuming this series sum equals to a real number,  $R$ , i.e.,  $\sum_{j=-\infty}^{\infty} 1/(1 + ij\omega\tau) = R$ , Eq. (31) can be written as

$$q_k^{(2)} = -KN_0 a^2 \bar{I}^{2N} R \frac{1}{1 + ik\omega\tau}. \quad (34)$$

Similarly, for the third-order interaction, based on Eq. (19), we have

$$\begin{aligned} q_k^{(3)} &= -a\bar{I}^N \frac{1}{1 + ik\omega\tau} \left[ p_k * q_k^{(2)} \right] = -a\bar{I}^N \frac{1}{1 + ik\omega\tau} \sum_{j=-\infty}^{\infty} q_j^{(2)} \\ &= KN_0 a^3 \bar{I}^{3N} R \frac{1}{1 + ik\omega\tau} \sum_{j=-\infty}^{\infty} \frac{1}{1 + ij\omega\tau} = KN_0 a^3 \bar{I}^{3N} R^2 \frac{1}{1 + ik\omega\tau}. \end{aligned} \quad (35)$$

Consequently, for the  $n$ -th-order interaction, we have

$$q_k^{(n)} = KN_0 (-1)^{n+1} a^n \bar{I}^{nN} R^{n-1} \frac{1}{1 + ik\omega\tau}. \quad (36)$$

In summary, based on Eqs. (24), (30), (34), (35), and (36), in physical situations where  $\lambda = 1$ ,  $q_k$  can be written as

$$\begin{aligned} q_k &= KN_0 \frac{1}{1 + ik\omega\tau} \sum_{n=1}^{\infty} (-1)^{n+1} a^n \bar{I}^{nN} R^{n-1} \\ &= KN_0 \frac{1}{1 + ik\omega\tau} (a\bar{I}^N - a^2 \bar{I}^{2N} R + a^3 \bar{I}^{3N} R^2 - \dots). \end{aligned} \quad (37)$$

By observing Eq. (37), we know that when pulse-train modulation is used in a GSOS microscope, the phase of the complex fluorescence harmonics  $q_k$  does not change due to the fixed complex factor  $1/(1 + ik\omega\tau)$  no matter how many orders of interaction are included or how high the excitation irradiance  $\bar{I}$  is. With this property, we can do (a) super-resolution microscopy and (b) FD-FLIM simultaneously. We can do (a) super-resolution microscopy because when we experimentally obtain the complex harmonics  $q_k$ , we can extract images of their magnitudes as

$$|q_k| = KN_0 \frac{1}{\sqrt{1 + (k\omega\tau)^2}} (a\bar{I}^N - a^2 \bar{I}^{2N} R + a^3 \bar{I}^{3N} R^2 - \dots). \quad (38)$$

Therefore, using the GSOS technique and the linear combination coefficients  $c_i$ , a super-resolution image can be obtained by linear combining  $M$  steps of images  $q_k$  at different powers. The

magnitude of the linear combination result,  $q_{k,M\text{-GSOS}}$ , is super-resolved with a  $\sqrt{M}$ -fold increase in spatial resolution over the DL. This is identical to the GSOS with sinusoidal modulation. We can do (b) FD-FLIM simultaneously because the phases of  $q_k$  and  $q_{k,M\text{-GSOS}}$  are invariant with excitation irradiances and can be easily obtained as

$$\angle q_k = \angle q_{k,M\text{-GSOS}} = -\arctan(k\omega\tau), \quad (39)$$

and therefore the lifetime  $\tau$  can be calculated as

$$\tau = -\frac{1}{k\omega} \tan(\angle q_k) = -\frac{1}{k\omega} \tan(\angle q_{k,M\text{-GSOS}}). \quad (40)$$

Note that even with pulse-train modulation, the GSOS microscopy can be easily returned to the SOS technique based on Eq. (37) with  $k = 0$ ,  $\omega = 0$ , and  $p_0 = 1$ . In this way,  $R$  becomes one for only one term (DC) exists in the summation, and therefore we have

$$F = q_0 = KN_0(a\bar{I}^N - a^2\bar{I}^{2N} + a^3\bar{I}^{3N} - \dots), \quad (41)$$

which is real and identical to the form in the SOS paper [8].

Here we perform simulations to acquire the dynamics of  $q_k$  numerically to see if the simulated results match the theoretical predictions above. The simulation approach and parameters are identical to the ones used in Sec. 5 and the results are presented in Fig. 2. With different excitation irradiances  $\bar{I}$ , the DC ( $q_0$ ),  $1\omega$  ( $q_1$ ), and  $2\omega$  ( $q_2$ ) fluorescence harmonics all show trajectories of straight lines with constant phases on the complex plane [Fig. 2(a)] and very similar magnitude and phase behaviors [Fig. 2(b)]. The phases of  $q_0$ ,  $q_1$ , and  $q_2$  are all invariant with excitation irradiances, as predicted by Eq. (39); their magnitudes exhibit a similar saturation behavior governed by Eq. (38), which is identical to the saturation of intensity in SOS microscopy [8]. Simulated magnitude and phase of complex PSFs of DC,  $1\omega$ , and  $2\omega$  harmonics for DL, 2-GSOS, and 3-GSOS are presented in Figs. 2(c) and 2(d). Identical to the simulated results for sinusoidal modulation, resolution improvements in magnitude PSFs of 2-GSOS and 3-GSOS over the DL can also be clearly seen for all DC,  $1\omega$ , and  $2\omega$  harmonics:  $g^{2N}(x)$  and  $g^{3N}(x)$  become the dominant terms for 2-GSOS and 3-GSOS, which corresponds to a  $\sqrt{2}$  and  $\sqrt{3}$  folds magnitude resolution improvements over  $g^N(x)$ , the dominant term in the DL [Fig. 2(c)]. Contrary to GSOS with sinusoidal modulation, whose phases become unpredictable under saturation [Fig. 1(d)], the simulated phase PSFs for GSOS with pulse-train modulation [Fig. 2(d)] (plotted are only the pixels with a magnitude larger than 0.1% of the peak value) demonstrate a constant phase regardless of whether the GSOS methods are used or not. Therefore the lifetime information  $\tau$  is preserved under the GSOS operation, which in turn permits super-resolution [magnitude, Eq. (38)] and FLIM [phase, Eq. (40)] imaging capabilities simultaneously.

## 7. Experimental demonstration of super-resolution FLIM by GSOS with pulse-train modulation

In this Section, we experimentally demonstrate the super-resolution FLIM capability enabled by GSOS with pulse-train modulation using a custom-built two-photon ( $N = 2$ ) FD-FLIM system. Note that one-photon (confocal,  $N = 1$ ) FD-FLIM is also compatible with GSOS. We only performed GSOS on the first fluorescence harmonic ( $1\omega$ ) image, i.e.,  $q_1$ , for the ease of implementation and higher signal-to-noise ratio (SNR). Higher harmonics  $q_k$  ( $k \geq 2$ ) could also be extracted using band pass filters and applied with GSOS methods in a similar manner, but the SNR performance could be poor due to their low intensity. In order to extract the first harmonic  $q_1$  from the fluorescence following the 80 MHz femtosecond pulse excitation, one could use a data acquisition (DAQ) device with a sampling rate at least higher than the Nyquist frequency (160 MHz) of the fundamental harmonic signal (80 MHz). However, this is challenging because

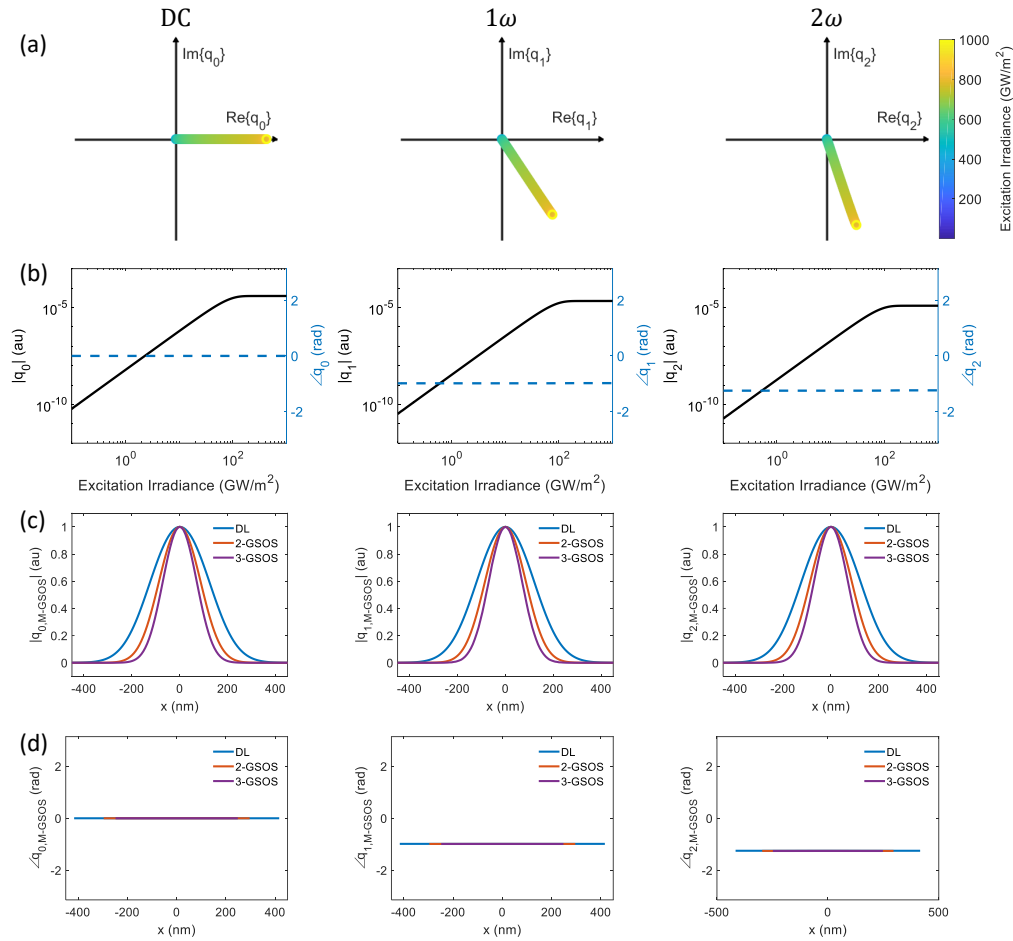


Fig. 2. Simulated results for GSOS microscopy with pulse-train modulation. (a) Complex trajectories and (b) magnitude and phase of fluorescence harmonics  $q_k$  with different excitation irradiances. (c) Magnitude and (d) phase of complex PSFs of diffraction-limited, two-step, and three-step GSOS microscopy.

(a) a DAQ card with a sampling rate higher than 100 MHz is very expensive, so the cost of the whole system could be prohibitive, and (b) in digital sampling, a ten-fold sampling rate is generally recommended to guarantee optimal performance, so one might need a DAQ card with an 800 MHz sampling frequency. To circumvent this difficulty, we designed a low-cost, high-performance homodyne detection method based on RF analog signal processing to extract the 80 MHz harmonic signal for super-resolution FD-FLIM imaging.

The experimental setup was an upgrade to the custom-built multiphoton FD-FLIM system we developed in [16, 17]. Figure 3 shows a block diagram of the homodyne FD-FLIM method that was added to our previous system. The intensity of a mode-locked Ti:sapphire laser (Spectra Physics Mai Tai BB, 710-990 nm, 100 fs, 80 MHz) was controlled by a half-wave plate and a polarizing beam splitter (PBS), which were used to variate the excitation laser power in different steps to perform GSOS microscopy. A power meter was used to measure the excitation power by monitoring a small fraction of the laser beam reflected by a glass slide; the measured powers were recorded to calculate the linear combination coefficients,  $c_i$ , in GSOS microscopy. A pair of galvo scanners (Thorlabs GVS002) controlled by a DAQ card (National Instruments PCI-6110)

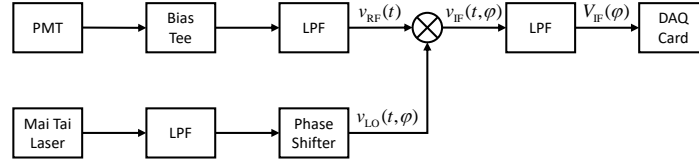


Fig. 3. Block diagram of the lifetime measurement method.

was used to generate scanning patterns. The excitation light was filtered through a longpass filter to block ambient light from entering the objective lens (Nikon CFI APO NIR, 40x, 0.8 NA). The 2PEF was epi-collected by the objective lens, reflected by a dichroic mirror, filtered through a set of bandpass and shortpass filters to eliminate residual excitation, and detected by a photomultiplier tube (PMT) (Hamamatsu H7422PA-40). The RF part of the PMT signal was extracted by a bias tee (Mini-Circuits ZFBT-282-1.5A+) and filtered by a low pass filter (LPF) (Mini-Circuits BLP-90+). On the other hand, the 80 MHz reference signal from the Ti:sapphire laser was filtered by a LPF (Mini-Circuits BLP-90+) to eliminate higher harmonics and phase shifted by a pair of phase shifters (Mini-Circuits JSPHS-150+). Note that each phase shifter could introduce a phase shift within  $\pi$  to the 80 MHz signal; therefore we connected them in series to introduce a total phase shift within  $2\pi$ . The phase shift was controlled by the bias voltage generated by an analog output port of another DAQ card (National Instruments PCIe-6323). The analog homodyne signal processing was performed on an RF mixer (Mini-Circuits ZAD-3H+). Note that signal amplifications were needed for the mixer to work at proper input power levels. As shown in Fig. 3, the mixer took the 80 MHz reference signal to its local oscillator (LO) port and the PMT signal to its RF port, and generated a mixed signal on its intermediate frequency (IF) port. The IF signal was then filtered by a LPF (Mini-Circuits BLP-1.9+) and the result was a pure DC signal acquired by the DAQ card (National Instruments PCI-6110). For each frame of image, four mixer images corresponding to four different phase shifts were acquired. The fluorescence lifetime image was then generated by simply applying basic matrix operations on these mixer images, which could be performed instantaneously. For  $M$ -GSOS,  $M$  frames of complex images obtained with different excitation powers were required; i.e.,  $4M$  mixer images were needed. If the time used to acquire each mixer image was  $T_0$ , then an  $M$ -GSOS operation would take  $4MT_0$ . The total data acquisition time could be reduced to  $MT_0$  by parallelizing the mixer image acquisition process; i.e., obtaining four mixer images simultaneously by splitting, phase shifting, and mixing the signals. All devices and measurements were controlled by a custom-written LabView (National Instruments) program.

Mathematically, the low-pass filtered PMT signal sent to the mixer's RF port can be written as  $q_1 \exp(i\omega t) + q_{-1} \exp(-i\omega t)$ , where  $\omega = 2\pi \times 80$  MHz. Since  $q_1 = q_{-1}^*$ , the signal can be simplified to  $v_{RF}(t) = 2\text{Re}\{q_1 \exp(i\omega t)\} = 2\text{Re}\{q_1\} \cos(\omega t) - 2\text{Im}\{q_1\} \sin(\omega t)$ . The phase  $\varphi$  of the 80 MHz reference signal sent to the mixer's LO port is controlled by the RF phase shifter:  $v_{LO}(t, \varphi) = \sin(\omega t + \varphi)$ . The output of the mixer on its IF port is  $v_{IF}(t, \varphi) = G v_{LO}(t, \varphi) v_{RF}(t) + D$ , where  $G$  is the conversion loss and  $D$  is the DC offset due to the circuit imbalance in the mixer [26]. After passing the LPF, the mixer's output becomes a DC signal:

$$V_{IF}(\varphi) = \frac{1}{T} \int_0^T v_{IF}(t, \varphi) dt = G [\text{Re}\{q_1\} \sin \varphi - \text{Im}\{q_1\} \cos(\varphi)] + D. \quad (42)$$

By varying the phase  $\varphi$  introduced by the phase shifter, we can obtain four measurements:  $V_{IF}(0) = -G \text{Im}\{q_1\} + D$ ,  $V_{IF}(0.5\pi) = G \text{Re}\{q_1\} + D$ ,  $V_{IF}(\pi) = G \text{Im}\{q_1\} + D$ ,  $V_{IF}(1.5\pi) = -G \text{Re}\{q_1\} + D$ . And we can get  $V_{IF}(\pi) - V_{IF}(0) = 2G \text{Im}\{q_1\}$ ,  $V_{IF}(0.5\pi) - V_{IF}(1.5\pi) = 2G \text{Re}\{q_1\}$ .

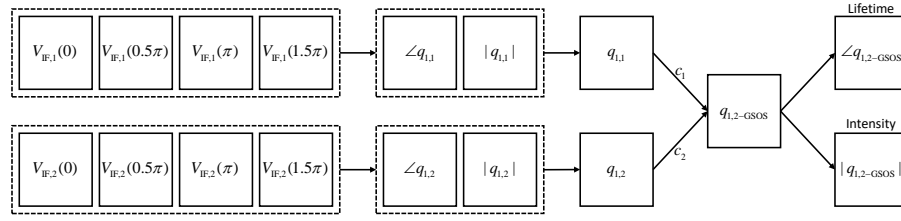


Fig. 4. Data acquisition and processing steps in two-step GSOS.

Therefore, the magnitude and phase of the first harmonic  $q_1$  can be extracted as

$$\angle q_1 = \arctan \left[ \frac{V_{IF}(\pi) - V_{IF}(0)}{V_{IF}(0.5\pi) - V_{IF}(1.5\pi)} \right], \quad (43)$$

$$|q_1| \propto \sqrt{[V_{IF}(\pi) - V_{IF}(0)]^2 + [V_{IF}(0.5\pi) - V_{IF}(1.5\pi)]^2}, \quad (44)$$

which are then combined as a complex value,  $q_1 = |q_1| \exp(i\angle q_1)$ . For  $M$ -GSOS, the measurement is repeated for  $M$  times with  $M$  different excitation powers,  $I_{01}, I_{02}, \dots, I_{0M}$ ; hence  $M$  steps of harmonics,  $q_{1,1}, q_{1,2}, \dots, q_{1,M}$ , are obtained based on the procedures described above. The harmonics are then linearly combined according to Eq. (27) with the coefficients  $c_i$  calculated using the excitation powers. The result of  $M$ -GSOS is an image with complex pixel values where its magnitude is a super-resolution image with a  $\sqrt{M}$ -fold increase in resolution over the DL and its phase can be converted to a fluorescence lifetime image using Eq. (40). The flow chart in Fig. 4 shows the data acquisition and processing steps used in 2-GSOS.

Before performing imaging, the system was calibrated using established fluorescence lifetime standards [coumarin 6 in methanol (2.3 ns), fluorescein in NaOH (4.0 ns), and rhodamine B in water (1.7 ns)] [27, 28] by adjusting the voltages applied to the phase shifters and ensuring that the measured lifetimes of these standards were identical to the values reported in the literature. The images were generated by the galvo scanners with  $400 \times 400$  pixels and a pixel width of 100 nm. The pixel dwell time was 20  $\mu$ s and the sampling frequency of the DAQ card was set to 5 MHz. Each mixer image took 3.2 s to acquire and was averaged for 20 times for the best SNR. The four mixer images for each GSOS step were acquired in parallel and the total data acquisition time for 2-GSOS was 128 s. Figure 5 shows the 2-GSOS super-resolution fluorescence lifetime images of fixed bovine pulmonary artery endothelial (BPAE) cells (Invitrogen FluoCells F36924) [29] obtained using our custom-built two-photon FD-FLIM system. MitoTracker Red CMXRos, Alexa Fluor 488 phalloidin, and DAPI were used to label the mitochondria, F-actin, and nuclei in the cells, respectively. We chose to image the BPAE cells as they contained sub-diffractive structures, such as F-actin and mitochondria, which could reflect the super-resolution capability of GSOS, and the lifetimes of the labeling dyes were well characterized. By imaging the cells we could also avoid the problems with sub-diffractive fluorescent beads, such as photobleaching and exploding due to heating effects. The excitation laser powers for the images of the first and second steps were  $I_{01} = 3.95$  mW and  $I_{02} = 4.61$  mW, where the powers were measured at the back aperture of the objective lens. The linear combination coefficients in GSOS microscopy were calculated according to Tab. 1 ( $N = 2$  for 2PEF):  $c_1 = 1$  and  $c_2 = -I_{01}^N / I_{02}^N = -0.7342$ . For the  $m$ -th step, two matrices  $\angle \mathbf{q}_{1,m}$  and  $|\mathbf{q}_{1,m}|$  were acquired based on Eqs. (43)-(44) and a complex matrix  $\mathbf{q}_{1,m} = |\mathbf{q}_{1,m}| \exp(i\angle \mathbf{q}_{1,m})$  was obtained. Therefore, based on Eq. (27), the two-step GSOS image was  $\mathbf{q}_{1,2\text{-GSOS}} = c_1 \mathbf{q}_{1,1} + c_2 \mathbf{q}_{1,2} = \mathbf{q}_{1,1} - 0.7342 \mathbf{q}_{1,2}$ .

Figure 5(a) shows the magnitude (normalized) and phase (ranging from  $-\pi/2$  to 0) images of  $\mathbf{q}_{1,1}$ ,  $\mathbf{q}_{1,2}$ , and  $\mathbf{q}_{1,2\text{-GSOS}}$ , respectively. Note that in the phase images only the pixels with a magnitude larger than 5% of the brightest pixel's magnitude are plotted because the pixels with



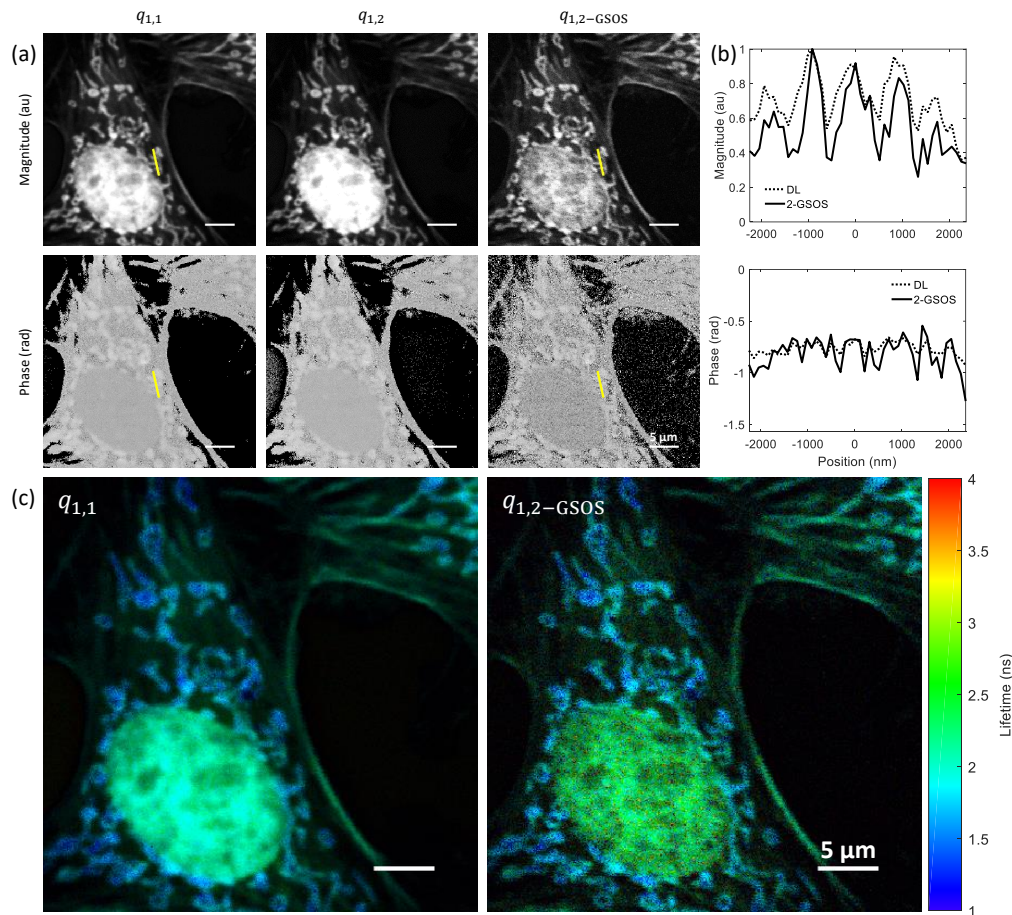


Fig. 5. Two-step GSOS microscopy generates super-resolution fluorescence lifetime images of fixed BPAE cells labeled with MitoTracker Red CMXRos (mitochondria), Alexa Fluor 488 phalloidin (F-actin), and DAPI (nuclei). (a) Magnitude and phase of the fundamental harmonic images of the first step ( $q_{1,1}$ ), the second step ( $q_{1,2}$ ), and their linear combination result ( $q_{1,2}$ -GSOS) in a two-step GSOS microscope. (b) Magnitude and phase profiles along the yellow lines in (a) showing that two-step GSOS is able to provide super-resolved magnitude images as well as preserve their lifetime (phase) information. (c) Composite images of the diffraction-limited ( $q_{1,1}$ ) and two-step GSOS ( $q_{1,2}$ -GSOS) harmonics, where the harmonics' magnitudes and the fluorescence lifetimes are mapped to the pixels' brightness and hue, respectively.

a low magnitude (non-fluorescent background) will demonstrate a random phase value due to noise. The two diffraction-limited images,  $q_{1,1}$  and  $q_{1,2}$ , show little difference in both magnitude and phase. However, the 2-GSOS image,  $q_{1,2}$ -GSOS, exhibits a clear resolution improvement in its magnitude over either one of the DL as well as preserves the lifetime information in its phase. The magnitude and phase of the intensity profiles of a few closely located mitochondria are shown in Fig. 5(b), where the mitochondria that cannot be easily resolved in the DL image can be clearly differentiated in the 2-GSOS one; while the mitochondrial structures are better resolved in the 2-GSOS magnitude image, their phases are intact (other than fluctuations due to noise) such that the lifetime information is preserved. Therefore, super-resolution (magnitude) FLIM (phase) images can be obtained simultaneously using the 2-GSOS methods, as predicted by the

theory in Sec. 6. To better illustrate the super-resolution FLIM capability of the 2-GSOS image over the DL one, their magnitude and phase are plotted compositely in pseudo-colored images in Fig. 5(c) where the magnitude is mapped to the pixels' brightness, and the phase mapped to the hue, respectively. The resolution improvement of the composite  $q_{1,2}$ -GSOS over  $q_{1,1}$  can be seen by observing features such as the closely packed mitochondria and the textures of the nuclei, for these features are clearer and better resolved in the 2-GSOS image. The lifetime information is preserved after the 2-GSOS processing for the color-coded lifetimes in the 2-GSOS image, such as the F-actin ( $\sim 2.3$  ns), the nuclei ( $\sim 2.0$  ns), and the mitochondria ( $\sim 1.5$  ns) are identical to the ones in the DL image. Moreover, the lifetime information is possibly enhanced in the 2-GSOS image for the lifetimes of the nucleus in the DL images are more uniform where many adjacent pixels share the same lifetime, while the 2-GSOS nucleus lifetimes demonstrate more details and less similarities among adjacent pixels.

## 8. Discussion and conclusion

Since GSOS is an extension of SOS, these two techniques share similar advantages and disadvantages. For example, both SOS and GSOS can be easily implemented on existing fluorescence intensity or FD-FLIM microscopes. Both methods can improve the imaging resolution by a factor of  $\sqrt{M}$  by linearly combining  $M$  steps of intensity or complex images obtained with different excitation powers, and theoretically the resolution improvement could be infinite. However, in practice, the resolution improvements in both techniques are limited by the SNR. As discussed in [8], the SOS image generated from more than two steps of raw images is generally unacceptable for its SNR is at least two orders of magnitude lower than a conventional image; the same problem also exists in GSOS microscopy. The SNR performance of GSOS could be even worse than SOS, since GSOS often relies on the harmonics  $q_k$  of a modulated fluorescence signal, which are generally weaker and noisier than the intensity of an unmodulated fluorescence signal used in SOS. To increase the GSOS/SOS performance, raw images with a high SNR are required. High SNR images could be obtained using long integration time, multiple exposures, or averaging, which could cause photobleaching or photodamage to the tissue. To address this issue, the strategy used in [8] to optimize the resolution and SNR simultaneously can be applied to both SOS and GSOS microscopy. Furthermore, both methods are based on a two-level fluorophore model; although the model can effectively describe the fluorophore saturation behavior, it does not take photobleaching into account, and therefore photobleaching should be avoided in GSOS/SOS.

Besides the similarities, GSOS is superior to SOS for SOS is just a special and the simplest case of GSOS. GSOS exhibits many benefits that are not available in SOS. For example, while SOS only works on conventional intensity-based fluorescence images, GSOS is suitable for both intensity- and modulation-based images where the additional lifetime information can be accessed; hence super-resolution and FLIM can be implemented simultaneously. Moreover, GSOS significantly expands the theoretical basis of SOS, which assumes a steady-state solution and uses Taylor expansion, by exploring the dynamics of the two-level fluorophore model and employs perturbation theory; therefore no steady-state assumption is made in GSOS and the results are more robust for practical situations.

In conclusion, we have presented GSOS, a novel microscopy technique that is capable of generating super-resolution and FLIM images simultaneously. The technique is developed based on exploring the dynamics of a two-level fluorophore model and using perturbation theory. We have shown that the previously demonstrated SOS microscopy is a special and the simplest case of the GSOS microscopy, for the GSOS method can be easily returned to the form in SOS microscopy. For both SOS and GSOS,  $M$  steps of raw images can be linearly combined to increase the imaging resolution by  $\sqrt{M}$ -fold, but only GSOS can extract the additional lifetime information while obtaining super-resolution images. We have also shown with theory

and simulations that both sinusoidal and pulse-train signals can be used as the excitation source in GSOS microscopy, where pulse-train modulation greatly simplifies the math in GSOS microscopy such that the lifetime information can be easily extracted. The super-resolution FLIM capability of a two-step GSOS microscopy with pulse-train modulation has been experimentally demonstrated with a cell sample on a custom-built two-photon FD-FLIM system based on RF analog signal processing. Finally, like SOS, GSOS is compatible with both one-photon (confocal) and multiphoton excitation fluorescence and does not require high excitation intensities. Therefore, due to the deep penetration of multiphoton excitation and the minimized damage of low excitation powers, GSOS could generate super-resolution lifetime images in deep tissues and living cells, provided that an acceptable SNR level could be obtained. As the first practice of combining a super-resolution technique with a fast and low-cost FD-FLIM method, the GSOS microscopy enables measurements of the microenvironment information at a size smaller than the diffraction limit.

### Funding

National Science Foundation (NSF) (CBET-1554516).

### Acknowledgments

Zhang's research was supported by the Berry Family Foundation Graduate Fellowship of Advanced Diagnostics & Therapeutics (AD&T), University of Notre Dame. The authors thank Stephen Leone of Mini-Circuits for providing advice on building the RF parts of the microscope.

### Disclosures

The authors declare that there are no conflicts of interest related to this article.